Measurements of the x-ray mass-attenuation coefficient and imaginary component of the form factor of copper

J. L. Glover, C. T. Chantler,* Z. Barnea, and N. A. Rae
School of Physics, University of Melbourne, Victoria 3010, Australia

C. Q. Tran
Department of Physics, La Trobe University, Victoria 3086, Australia

D. C. Creagh
Division of Science and Design, University of Canberra, Australian Capital Territory 2601, Australia

D. Paterson
Australian Synchrotron, Clayton, Victoria 3168, Australia

B. B. Dhal
Centre for Materials Research, Curtin University of Technology, Western Australia 6845, Australia
(Received 11 September 2008; published 13 November 2008)

The x-ray mass-attenuation coefficient of copper was measured at 108 energies between 5 and 20 keV using synchrotron radiation. The measurements are accurate to between 0.09 and 4.5 %, with most measurements being accurate to better than 0.12%. The imaginary component of the form factor of copper was also determined after subtracting the attenuation contribution due to scattering. Measurements were made over an extended range of experimental parameter space, allowing us to correct for several systematic errors present in the data. These results represent the most extensive and accurate dataset of their type for copper in the literature and include the important and widely studied region of the *K*-edge and x-ray absorption fine structure. The results are compared with current theoretical tabulations as well as previous experimental measurements and expose inadequacies in both.

DOI: 10.1103/PhysRevA.78.052902 PACS number(s): 32.80.Aa, 61.05.cj, 78.20.Ci, 78.70.Dm

I. INTRODUCTION

X-ray attenuation is widely used to investigate everything from broken bones [1] to the structure of atoms [2]. Direct measurements of the attenuation coefficient can be used to investigate the bonding and local structure of materials as in x-ray absorption fine structure (XAFS) and near-edge structure [3]. Secondary processes such as Auger electron emission and fluorescence radiation are also also used to investigate biological, molecular, surface and solid state properties [4,5]. The diverse range of physical processes involved in x-ray attenuation are reflected in the many techniques it has spawned.

The x-ray mass-attenuation coefficient and form factor can be calculated using atomic wave functions and quantum electrodynamics. High-accuracy experimental measurements of the mass-attenuation coefficient provide a critical test for these theoretical approaches. The two theoretical tabulations of x-ray form factors and mass-attenuation coefficient s recommended by the National Institute of Standards and Technology (NIST) are FFAST [6,7] and XCOM [8]. Significant discrepancies exist between the two tabulations, particularly in the region of absorption edges [9]. Additionally, previous high-accuracy absolute measurements of the mass-attenuation coefficient have been discrepant from both tabulations by up to 10% [9–12].

There have been numerous previous measurements of the x-ray mass-attenuation coefficient of copper using a variety of techniques and x-ray sources over a wide range of energies. Many of these measurements were published without estimates of their uncertainties, but of those that did include such estimates, most reported experimental uncertainties in the 0.5 to 3 % range (see Table I).

Figure 1 plots all the measurements of copper available to us that included uncertainty estimates in the energy range of interest. Table I summarizes the details of these experiments, including the x-ray source, energy range, and reported accuracy. The measurements disagree with one another by up to 20% and ten standard deviations.

The most accurate previous determination of the mass-attenuation coefficient of copper was that of Chantler *et al.* [13] which covers 84 energies between 8.9 and 20 keV. It is instructive to compare the results of the Chantler dataset with the five datasets from Table I which include more than two measurements between 8.9 and 20 keV. Only one of those five datasets, that of Murty *et al.* [14], agrees with Chantler *et al.* to within two standard deviations, and significant discrepancies exist between the Chantler dataset and the remaining four. The strong disagreement between different experimental determinations of the mass-attenuation coefficient indicates the presence of unquantified systematic errors and an underestimation of experimental error bars.

Frustrated by discrepancies between reported values of the x-ray mass-attenuation coefficient, the International

*chantler@unimelb.edu.au

TABLE I. Previous measurements of the mass-attenuation coefficient of copper between 5 and 21 keV. Some of the references in this table extend over a larger energy range; where that is the case, the information in the table below is true of the subset of thedata in the 5 to 21 keV range.

		Energies (keV)		% Accuracy	
Authors (Ref.)	X-ray source	Range	No.	Range	Median
Hopkins [15]	X-ray tube	6–21	18	0.7–3.9	3.2
Cooper [16]	X-ray tube	5–18	5	0.8–1.7	1.6
Bearden [17]	X-ray tube	8–20	5		1.0
Hughes *et al.* [18]	Electron microprobe	5–10	9		1.0
Parthasaradhi and Hansen [19]	Radioactive isotope	5–21	6	1.9–2.2	2.0
Murty *et al.* [14]	Radioactive isotope	5–20	6	0.9–1.2	1.0
Rao and Shahnawaz [20]	Radioactive isotope	6–15	2	1.9–1.9	1.9
Puttaswamy *et al.* [21]	Radioactive isotope	5–15	4	0.9–1.1	1.0
Nathuram *et al.* [22]	Radioactive isotope	5–21	4	0.8–1.5	1.0
Unonius and Suortti [23]	X-ray tube	5–11	17	0.5–1.8	1.1
Dachun *et al.* [24]	Proton induced fluorescence	5–20	27	0.9–3.1	1.0
Tajuddin *et al.* [25]	Radioactive isotope	13–18	2	3.2–4.0	3.5
Sandiago *et al.* [26]	Radioactive isotope	5–15	5		3.0
Chantler *et al.* [13]	Synchrotron	8.9–20	84	0.27–0.7	0.33

Union of Crystallography inaugurated the X-ray Attenuation Project. The aim of this project was to establish reliable and accurate techniques for measuring the x-ray mass-attenuation coefficient that "minimize systematic error" [27,28]. One of their conclusions was that "systematic errors are present in tables which are based on experimental data" and pointed to harmonic contamination, detector effects such as dead time, and excessive beam divergence as possible culprits [27].

Although systematic errors can be reduced by careful consideration of the experimental setup, they cannot be completely eliminated. The effect of systematic contributions to experimental measurements can be assessed by making measurements over an extended range of experimental parameter space. The magnitude of these systematic effects can then be determined and an appropriate correction and uncertainty contribution can be applied to the data.

In this article we present measurements of the x-ray mass-attenuation coefficient of copper at 108 energies between 5 and 20 keV. The results are accurate to between 0.09 and 4.5 % with most measurements being accurate to better than 0.12%. The imaginary component of the form factor of copper was also determined from the mass-attenuation coefficient after subtraction of the scattering contribution and is accurate to between 0.095 and 4.5 %.

This paper presents measurements of the x-ray mass-attenuation coefficient and derivation of the imaginary component of the form factor of copper, and represents a threefold improvement in accuracy over the previous measurements cited in this paper. Below the absorption edge, between 5 and 8.9 keV, this work is more than five times more accurate than the previous measurements [23]. These results have low enough uncertainty to critically test the different theoretical tabulations of form factors and mass-attenuation coefficient s and will also be useful as a standard in their own right for XAFS, crystallographic, and medical applications.

II. EXPERIMENTAL DETAILS

The mass-attenuation coefficient of copper was measured to high accuracy using the X-ray extended range technique (XERT) [13,29]. The measurements were made using bending-magnet synchrotron radiation at beamline 20B of the Photon Factory in Japan.

A. Experimental technique

The XERT is a technique for high-accuracy measurement of mass-attenuation coefficients, form factors and x-ray absorption fine structure (XAFS). It has been used on a variety of sample types and has produced the most accurate measurements of the mass-attenuation coefficient in the literature [9].

An essential prerequisite for high-accuracy measurements of this type is the careful consideration of systematic errors, such as those due to scattering, fluorescence and the attenuation of the detectors and air path [30]; these effects are inherent in all attenuation measurements made in transmission geometry. The use of a synchrotron source and crystal monochromation lead to systematic errors due to the finite energy bandwidth of the x rays [31] and the presence of harmonic energies [32].

In the XERT, measurements are carried out over an extended range of experimental-parameter space in order to test for systematic errors affecting the measurements. In this experiment, the parameters varied over an extended range were sample thickness, x-ray energy, measurement time, detector linearity, sample orientation, and detector angular acceptance. Probing these parameters over an extended range allowed us to recognize and correct several systematic errors that were present in our data (see Sec. V).

A schematic of the experimental setup is shown in Fig. 2. The energy of the x-ray beam was selected by a detuned

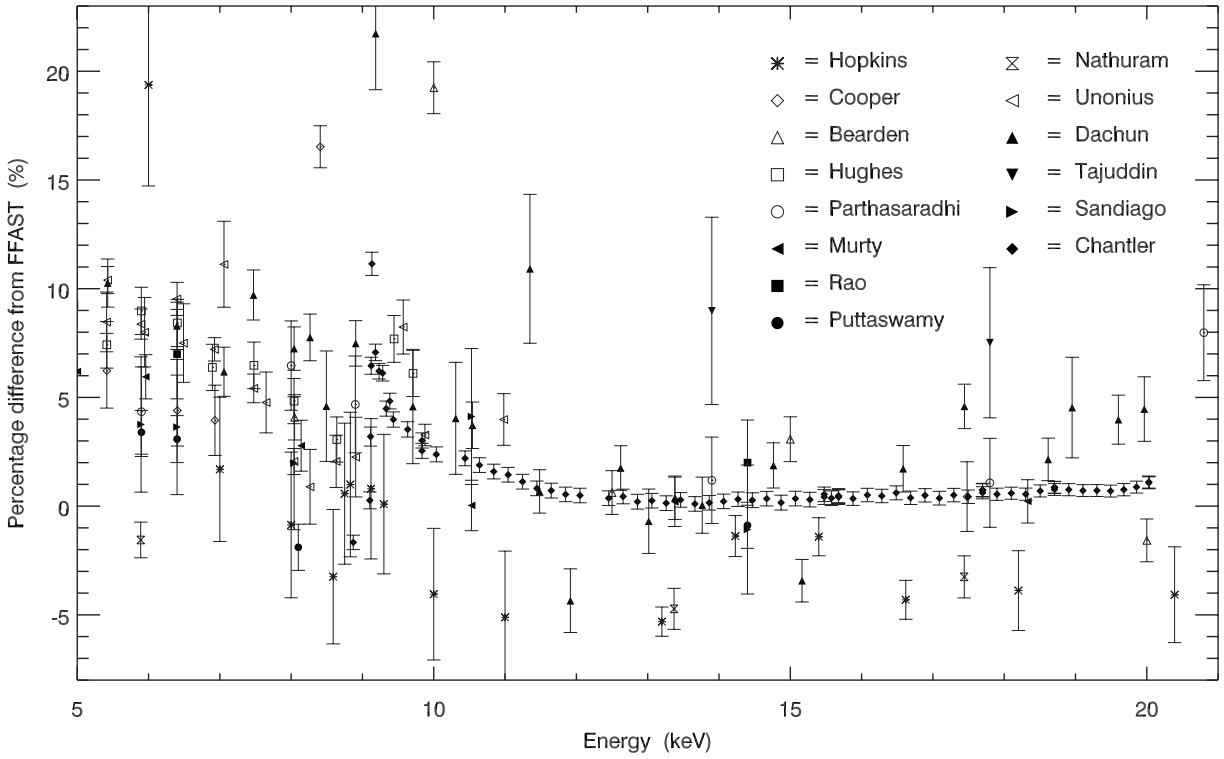

FIG. 1. A comparison of past measurements of the mass attenuation coefficient of copper between 5 and 21 keV. The measurements are plotted as a percentage difference from the FFAST tabulation of mass-attenuation coefficients and form factors [6,7]. Measurements at the copper *K* edge and the first three XAFS peaks (between 8.95 and 9.05 keV) have been excluded. There is one point outside the ordinate range of the graph; a measurement by Nathuram at 20.160 keV was 17.6% less than the tabulated FFAST value (measurement uncertainty 1.4%).

double-crystal monochromator utilizing a monolithic silicon 111 crystal. The beam energy was accurately determined using a powder diffractometer [33] and two powder sample standards from the National Institute of Standards and Technology (NIST) [34,35].

Matched 186 mm ion chambers were placed upstream and downstream of the copper samples and run in serial-flow mode using nitrogen gas. The use of matched ion chambers ensured maximum correlation between the upstream and downstream detectors and helped to correctly normalize synchrotron intensity instability—leading to an improvement in accuracy [36,37]. Each measurement was repeated at least ten times so that a well-defined precision could be associated with each measurement.

The sample stage held three copper foils and was configured so that it could translate along and rotate about the horizontal and vertical axes perpendicular to the beam. Accurate translational control was essential so that the synchrotron beam could be positioned on the sample reliably and reproducibly. Rotating the sample stage allowed us to detect and correct for any small misalignment of the sample compared to the ideal orientation perpendicular to the beam.

Daisy wheels [32] were mounted between the sample stage and the two ion chambers. Three circular apertures were cut into the perimeter of the daisy wheels, subtending solid angles of 1.05, 4.07, and 25.4 msr (millisteradian). These apertures were used to collimate the scattered and fluorescent photons thereby controlling the angular acceptance of the detectors. Fifteen aluminium foils were mounted around the perimeter of the daisy wheels and had thicknesses that varied over several orders of magnitude. These foils extended the measured thickness range and therefore provided additional information about the thickness dependence of any systematic errors.

B. Samples

The six copper-foil samples used in the experiment were supplied by Goodfellow and ranged in thickness from 5 to 100 μm. The foils were securely mounted in bevelled Perspex holders that tightly held the edges of the samples. Table II lists the sample configuration for each energy range.

The manufacturer quoted purity was 99.99% for all foils except the 5 μm foil which was 99.97%. The effect of im-

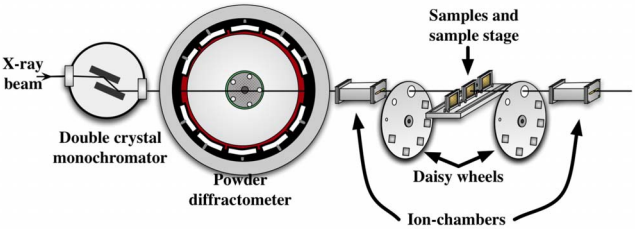

FIG. 2. (Color online) A typical setup used during an experiment utilising the XERT. This diagram is not to scale.

TABLE II. The nominal thicknesses of the copper-foil samples used during the experiment. The samples were changed at 16, 8.5, 8, and 6 keV. Samples that had $[\rho t]$ determined using the full-foil mapping technique are indicated in bold.

Energy range (keV)	Sample position 1	Sample position 2	Sample position 3
20–18	100 μm (a)	100 μm (b)	30 μm
18–16	100 μm (a)	10 μm	30 μm
16–8.5	15 μm	10 μm	5 μm
8.5–8	15 μm	100 μm (b)	5 μm
8–6	15 μm	10 μm	30 μm
6–5	15 μm	10 μm	5 μm

purities on the measured mass-attenuation coefficient s is discussed in Sec. V A.

The mass of each sample was determined by repeated weighing on a microgram scale (resolution 1 μg) to an accuracy of between 0.001 and 0.04 %. The areas of the samples (nominally 25 by 25 mm) were measured using a Mitutogo PJ300 optical comparator (resolution 5×5 μm^2) to an accuracy of between 0.03 and 0.04 %. The mass and area measurements were used in Sec. IV for the absolute determination of the mass-attenuation coefficient.

III. THE RELATIVE MASS-ATTENUATION COEFFICIENT

The relative mass-attenuation coefficient $[\frac{\mu}{\rho}][\rho t]$ of a sample is measured in transmission geometry using the Beer-Lambert equation

$$\left[\frac{\mu}{\rho}\right][\rho t] = -\ln\left(\frac{I}{I_0}\right). \tag{1}$$

I_0 and I are the ion chamber current measured by the upstream and downstream detectors, respectively. These quantities were measured simultaneously in order to normalize any fluctuations in the intensity of the synchrotron beam. The treatment of dark current and the assignment of uncertainties to the relative mass-attenuation coefficient were similar to those reported in Ref. [9].

Equation (1) can be solved to determine the relative mass-attenuation coefficient of all the matter between the front of the upstream ion chamber and the front of the downstream ion chamber. In order to remove the contributions to the attenuation due to the airpath and detectors, two measurements must be made. Measurements were taken with the sample in place and with the sample removed and then the relative mass-attenuation coefficient of the sample was calculated using [9,13]

$$\left[\frac{\mu}{\rho}\right][\rho t]_S = \left[\frac{\mu}{\rho}\right][\rho t]_{S+\mathrm{IC1}+A} - \left[\frac{\mu}{\rho}\right][\rho t]_{\mathrm{IC1}+A}, \tag{2}$$

where the subscripts IC1, *A*, and *S* refer to the upstream ion chamber, airpath, and sample, respectively. Calculating the attenuation of the sample using Eq. (2) corrects for any small differences in efficiency and electronic gain of the two ion chambers.

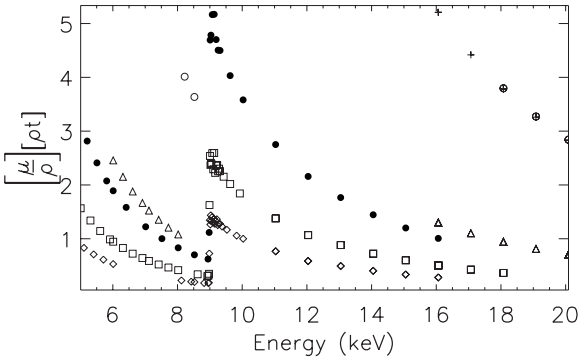

FIG. 3. Measured values of the relative mass-attenuation coefficient are plotted against energy. In order to make the plot clearer, not all energies are plotted. Each symbol is associated with a particular foil of a given nominal thickness ◇: 5 μm; □: 10 μm; ●: 15 μm; △: 30 μm; +: 100 μm (a); ○: 100 μm (b).

A. Extended energy measurements

Measurements of the relative mass-attenuation coefficient were made at 108 energies between 5 and 20 keV. This energy range included the copper *K* edge at 8.9 keV and the associated fine structure (XAFS) just above it. In these regions, measurements were made with smaller energy steps so that the fine structure was well characterized.

Figure 3 plots the measured relative mass-attenuation coefficient against energy. At each energy, measurements of at least three sample thicknesses were made. Sample changes were coordinated so that, where possible, the relative attenuation satisfied an extended Nordfors criterion ($0.5\leqslant[\frac{\mu}{\rho}][\rho t]\leqslant5$) [13,38].

B. Determining the photon energies

Measurements of the mass-attenuation coefficient require an accurate and robust method to determine the energy of the beam used in the attenuation measurements. We determined the energy using a powder diffractometer and two powder standards with well characterized lattice parameters. The two NIST powder diffraction standards–Si (640b) [34] and LaB_6(660) [35]–were chosen because they were the most accurate powder diffraction standards available.

A nominal x-ray energy was assigned to each measurement based on the encoder reading from the motor controlling the angular movement of the monochromator crystals. While these encoder energies have been shown to be precise, they typically contain offset and scaling errors and do not provide an accurate measurement of the x-ray energy [39].

Energy calibration measurements were typically made every 1 to 2 keV but were not performed at every energy where an attenuation measurement was made. The discrepancy between the nominal and calibrated energies displayed a linear relationship with the nominal x-ray energy being up to 70 eV lower than the calibrated energy (see Fig. 4). The energy of the *K* edge is an important parameter in XAFS and it is notable that the nominal energy was incorrect by 20 eV at the edge. A detailed description of the energy calibration performed for this experiment is given in Ref. [39].

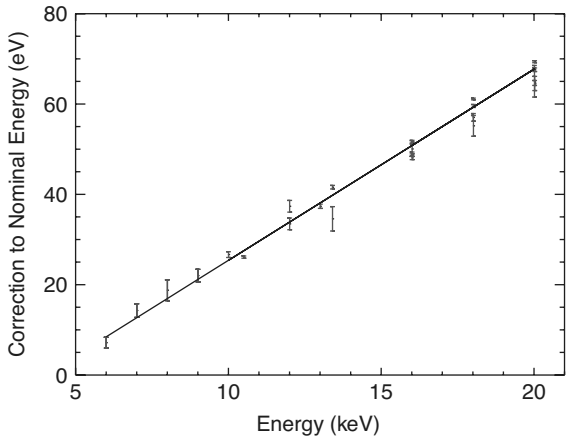

FIG. 4. The difference between the calibrated x-ray energy and the nominal x-ray energy is plotted. The calibrated energies were determined using powder diffraction measurements performed on two standard powders. Below 11 keV only the LaB_6 powder diffraction patterns produced useful results.

A linear model was used to describe the difference between the nominal and calibrated energies; the parameters of this model were determined using a least squares fitting procedure. The best-fit parameters were used to determine the calibrated energy of every measurement in the experiment. The accuracy of the resultant interpolated, calibrated x-ray energies was between 0.3 and 0.6 eV. A full tabulation of the x-ray energies and their associated uncertainties is given in Table III.

IV. ABSOLUTE DETERMINATION OF THE MASS-ATTENUATION COEFFICIENT OF COPPER

The x-ray mass-attenuation coefficient was determined on an absolute scale (cm^2/g) using the full-foil mapping technique [40,41] for the two thickest foils. The determination was made at the highest possible energy in order to minimise systematic errors associated with the absorption edge and harmonics. The full-foil mapping technique has been described in detail elsewhere [40,41].

The process used here to determine the absolute mass-attenuation coefficient can be summarized as follows. The average mass per unit area of the sample $[\rho t]_{\text{ave}}$ was determined accurately (0.04%) by dividing the mass of the sample by its area. Measurements of the attenuation were then performed during a raster scan across 195 points on the surface of the sample (see Fig. 5). After removing the contribution to the attenuation made by the sample holder, the results of the full-foil mapping were used to compute the average relative mass-attenuation coefficient of the sample $[\frac{\mu}{\rho}][\rho t]_{\text{ave}}$. This was then divided by the average mass per unit area to determine the absolute mass-attenuation coefficient.

A. Removal of the holder attenuation

All of the copper foils were mounted in bevelled Perspex holders. At some points measured during the full-foil mapping the beam passed through the holder, contributing up to a

TABLE III. The mass-attenuation coefficient as well as the form factor of copper are tabulated at a 108 energies between 5 keV and 20 keV. These quantities are listed along with the one standard deviation uncertainty in the least significant digit(s), which are given in brackets. The values of f'' between 8.95 keV and 9.5 keV are affected by solid-state effects.

Energy (keV)	$[\frac{\mu}{\rho}]$ (cm^2/g)	$\frac{\sigma_{[\mu/\rho]}}{[\mu/\rho]}$ (%)	f'' e/atom
5.0053(6)	193.5(3)	0.136	1.440(2)
5.1060(6)	182.97(19)	0.106	1.3883(15)
5.2063(6)	173.10(18)	0.101	1.3383(14)
5.3069(6)	164.00(16)	0.095	1.2916(13)
5.4073(6)	155.57(15)	0.095	1.2475(12)
5.5079(6)	147.69(14)	0.095	1.2055(12)
5.6085(6)	140.24(14)	0.100	1.1648(12)
5.7089(6)	133.47(13)	0.099	1.1276(12)
5.8096(6)	127.08(14)	0.112	1.0917(13)
5.9100(6)	121.13(14)	0.112	1.0578(12)
6.0105(6)	115.76(11)	0.093	1.0274(10)
6.1111(6)	110.77(11)	0.094	0.9989(10)
6.2114(6)	106.16(11)	0.100	0.9724(10)
6.3117(5)	101.41(10)	0.094	0.9432(9)
6.4123(5)	96.95(9)	0.095	0.9153(9)
6.5128(5)	92.62(9)	0.096	0.8874(9)
6.6130(5)	88.52(8)	0.094	0.8605(9)
6.7136(5)	84.83(9)	0.109	0.8365(10)
6.8142(5)	81.23(9)	0.108	0.8122(10)
6.9148(5)	78.46(8)	0.106	0.7957(10)
7.0151(5)	74.78(7)	0.098	0.7685(9)
7.1156(5)	71.80(7)	0.096	0.7478(8)
7.2160(5)	68.98(7)	0.094	0.7280(8)
7.3168(5)	66.32(7)	0.098	0.7090(8)
7.4171(5)	63.77(7)	0.105	0.6906(8)
7.5174(5)	61.30(6)	0.095	0.6721(8)
7.6180(5)	59.04(7)	0.110	0.6555(9)
7.7184(5)	56.89(6)	0.105	0.6394(8)
7.8190(5)	54.80(5)	0.098	0.6233(8)
7.9195(5)	52.78(5)	0.097	0.6075(8)
8.0200(4)	50.95(5)	0.100	0.5933(8)
8.1204(4)	49.18(5)	0.106	0.5794(8)
8.2212(4)	47.48(5)	0.098	0.5658(8)
8.3215(4)	45.90(4)	0.097	0.5531(7)
8.4222(4)	44.38(4)	0.101	0.5407(8)
8.5220(4)	42.95(4)	0.097	0.5289(8)
8.6226(4)	41.50(4)	0.104	0.5166(8)
8.7231(4)	40.10(5)	0.122	0.5045(9)
8.8236(4)	38.76(4)	0.109	0.4928(8)
8.9229(4)	37.91(4)	0.104	0.4870(8)
8.9431(4)	38.06(10)	0.268	0.4902(15)
8.9529(4)	38.32(11)	0.277	0.4944(16)

TABLE III. (*Continued.*)

Energy (keV)	$[\frac{\mu}{\rho}]$ (cm^2/g)	$\frac{\sigma_{[\mu/\rho]}}{[\mu/\rho]}$ (%)	f'' e/atom
8.9578(4)	38.61(10)	0.258	0.4985(15)
8.9629(4)	39.04(13)	0.331	0.5046(19)
8.9680(4)	39.9(2)	0.517	0.517(3)
8.9732(4)	41.5(5)	1.297	0.539(7)
8.9782(4)	58.6(7)	1.218	0.771(10)
8.9830(4)	157.2(5)	0.340	2.108(7)
8.9880(4)	193.2(7)	0.378	2.598(10)
8.9930(4)	282.3(5)	0.165	3.810(6)
8.9981(4)	293.6(7)	0.232	3.966(9)
9.0032(4)	311.0(5)	0.171	4.204(7)
9.0084(4)	291.7(6)	0.189	3.944(8)
9.0134(4)	276.6(5)	0.187	3.741(7)
9.0183(4)	288.7(5)	0.178	3.908(7)
9.0232(4)	309.3(4)	0.116	4.190(5)
9.0283(4)	315.4(5)	0.155	4.277(7)
9.0332(4)	295.2(4)	0.139	4.003(6)
9.0384(4)	287.3(3)	0.120	3.898(5)
9.0436(4)	291.0(3)	0.102	3.951(4)
9.0486(4)	291.9(3)	0.119	3.965(5)
9.0537(4)	296.0(4)	0.129	4.024(5)
9.0635(5)	306.2(5)	0.151	4.167(6)
9.0735(5)	318.0(5)	0.161	4.334(7)
9.0836(5)	298.3(4)	0.149	4.068(6)
9.0935(5)	285.3(3)	0.114	3.894(5)
9.1034(5)	279.7(4)	0.144	3.822(6)
9.1138(5)	294.4(4)	0.132	4.028(5)
9.1237(5)	299.0(4)	0.146	4.095(6)
9.1334(5)	317.7(5)	0.150	4.359(7)
9.1438(5)	306.7(5)	0.165	4.212(7)
9.1539(5)	279.8(5)	0.181	3.844(7)
9.1638(5)	271.3(5)	0.168	3.730(6)
9.1738(5)	289.9(3)	0.110	3.992(4)
9.1841(5)	290.8(3)	0.112	4.009(5)
9.1941(5)	288.2(4)	0.125	3.978(5)
9.2038(5)	291.8(4)	0.122	4.031(5)
9.2140(5)	298.8(4)	0.146	4.134(6)
9.2241(5)	291.1(5)	0.160	4.031(7)
9.2340(4)	278.3(3)	0.094	3.858(4)
9.2440(5)	274.5(3)	0.106	3.808(4)
9.2541(5)	275.6(3)	0.113	3.828(4)
9.2643(5)	277.3(3)	0.122	3.855(5)
9.2742(5)	280.1(3)	0.117	3.899(5)
9.2842(5)	281.5(3)	0.104	3.923(4)
9.2945(5)	282.5(3)	0.110	3.941(4)
9.3045(5)	280.9(4)	0.150	3.923(6)
9.3144(5)	276.1(3)	0.120	3.860(5)
9.3251(5)	272.7(3)	0.101	3.816(4)

TABLE III. (*Continued.*)

Energy (keV)	$[\frac{\mu}{\rho}]$ (cm^2/g)	$\frac{\sigma_{[\mu/\rho]}}{[\mu/\rho]}$ (%)	f'' e/atom
9.3758(4)	269.1(2)	0.091	3.786(4)
9.4257(4)	263.2(2)	0.093	3.723(4)
9.4758(4)	257.8(2)	0.092	3.665(3)
9.5268(4)	255.4(3)	0.099	3.651(4)
9.6267(4)	246.6(3)	0.126	3.561(5)
9.7275(4)	238.5(2)	0.092	3.480(3)
9.8279(4)	231.8(2)	0.093	3.417(3)
9.9282(4)	225.3(2)	0.091	3.353(3)
10.0284(3)	219.0(2)	0.094	3.294(3)
11.0334(3)	168(6)	3.417	2.78(10)
12.0385(3)	131(6)	4.384	2.36(10)
13.0442(3)	108.00(10)	0.096	2.104(2)
14.0496(3)	88.42(9)	0.100	1.853(2)
15.0559(3)	73.42(7)	0.098	1.6466(18)
16.0619(4)	61.60(6)	0.093	1.4715(16)
17.0699(4)	52.20(5)	0.093	1.3233(15)
18.0768(5)	44.69(4)	0.094	1.1977(13)
19.0836(5)	38.51(4)	0.099	1.0878(12)
20.0885(6)	33.45(3)	0.092	0.9927(10)

further 15% to the attenuation. Figure 5 plots the value of the relative mass-attenuation coefficient across the surface as measured during the raster scan of the foil. The profile of the circularly bevelled holder attenuation is clearly visible.

The effect of the attenuation of the holder is removed with the aid of a model of the attenuation of the sample and holder. The model is analogous to that used in Ref. [40], where the sample is modeled as a wedge-shaped block (with y undulation) and the holder is modeled from its design

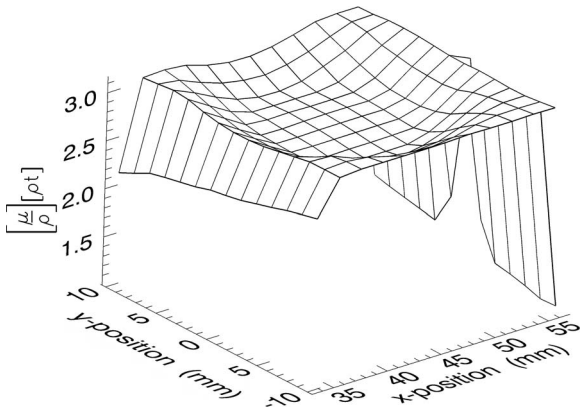

FIG. 5. $[\frac{\mu}{\rho}][\rho t]$ of the surface and holder combination was measured during a raster scan across the surface of the sample. The relative mass-attenuation coefficient is plotted on the vertical axis; the horizontal axes represent the position of the x-ray beam. The shape of the bevelled holder can be seen in the attenuation.

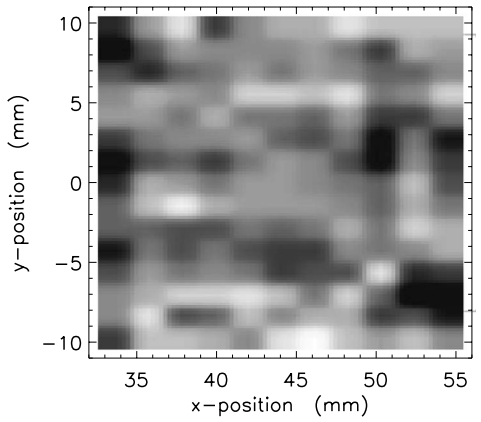

FIG. 6. The residuals resulting from the fit of the areascan data to the model of the attenuation of the sample and holder. Black areas are those that differ from the model by the greatest magnitude while white areas are those in best agreement. The absence of circular artifacts indicates that the holder removal process was successful.

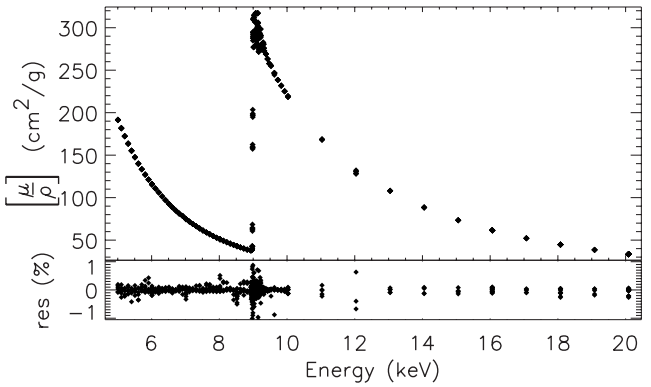

FIG. 7. The mass-attenuation coefficient of copper is plotted against energy. Each sample and aperture measurement is plotted separately in the top panel. A weighted mean was calculated at each energy and the residuals from that mean are plotted in the lower panel of the figure. Some systematic discrepancies can be seen, particularly at the edge where they reach 8% (the *y* axis has been cropped).

drawings. The model was fitted to the full-foil mapping data and the results of the fit were used to subtract the contribution to the attenuation made by the holder.

The residuals resulting from the model fit to the measured attenuation of the sample and holder combination are shown in Fig. 6. The bevel has considerable circular structure and the absence of circular artifacts from the residuals indicates that the beveled holder was modeled successfully and that the attenuation of the holder removed.

B. Determination of $[\frac{\mu}{\rho}][\rho t]_{\text{ave}}$

A 2 mm$\times$1.5 mm synchrotron beam was used to measure the attenuation of most of the sample. Some areas at the edge of the sample were not measured during the raster scan. An estimate of the attenuation of every point on the sample is required to accurately determine the average attenuation. Since the attenuation of the sample is position dependent, we must calculate a population mean rather than relying on sampling techniques. The average attenuation was calculated from the full-foil mapping data

$$\left[\frac{\mu}{\rho}\right][\rho t]_{\text{ave}} = \frac{1}{A_T}\sum_x \left[\frac{\mu}{\rho}\right][\rho t]_x A_x, \tag{3}$$

where $[\frac{\mu}{\rho}][\rho t]_x$ is the attenuation of the sample in the region with its center at x, and A_x is the area of this region. A_T is the total area of the sample. This sum must be performed over a set of regions that form a complete partition of the sample area.

A small region at the corners and on the edge of the sample was not directly measured during the raster scan of the sample; the attenuation of these regions was taken from the model described earlier. The uncertainty associated with these points is of a similar magnitude to the residuals (1–2 %). The directly measured points had an uncertainty that was always less than 0.1%.

Using the method outlined above $[\frac{\mu}{\rho}][\rho t]_{\text{ave}}$ at an energy of 20 088 eV was calculated to be 2.8192 ± 0.0034 for sample 100 μm (a); 2.8145 ± 0.0036 for sample 100 μm (b).

C. Absolute mass-attenuation coefficient

We can now determine the mass-attenuation coefficient of copper at 20 088 eV. This is done by dividing $[\frac{\mu}{\rho}][\rho t]_{\text{ave}}$ by $[\rho t]_{\text{ave}}$. The uncertainty in the determined value is dominated by the uncertainty associated with undersampling. The mass-attenuation coefficient of the two samples was determined to be 33.406 ± 0.042 cm^2/g for sample 100 μm (a); 33.503 ± 0.044 cm^2/g for sample 100 μm (b).

These values are in reasonable agreement and were combined to yield a final determination of the mass-attenuation coefficient of copper at 20 088 eV of 33.453 ± 0.031 cm^2/g. This corresponds to an accuracy of 0.092%.

D. Thickness propagation

The absolute determination of the mass-attenuation coefficient of copper can be used to convert the relative attenuation data from Sec. III into data on an absolute scale (cm^2/g). This process can be thought of as a scaling or equivalently as a determination of the integrated column density $[\rho t]$ of each sample.

The full-foil mapping technique was performed on the two thickest samples; the integrated column density of the other samples was determined by demanding self consistency. The remaining integrated column densities and their associated uncertainties were determined using a least squares fitting routine that minimised the χ^2 deviation between the $[\frac{\mu}{\rho}]$ measurements taken on the different samples.

Figure 7 plots the determined mass-attenuation coefficient and its residuals. The clear influence of systematic errors can be seen in the residual plot, particularly in the edge region and at 12 keV. Correcting for these systematic errors will be the subject of Sec. V.

V. CORRECTING FOR SYSTEMATIC ERRORS

We observe a number of systematic errors affecting our determination of the mass-attenuation coefficient. The systematic errors were identified by their dependence on experimental parameters such as foil thickness, aperture size, and energy.

A. Impurities

The copper foils used in the experiment were nominally 99.99% pure except for the 5 μm sample which was 99.97% pure. The manufacturer lists a typical assay of impurities to be 2–100 ppm lead, 4–50 ppm silver, 1–100 ppm potassium, and 1–25 ppm calcium. All other contaminants (aluminium, bismuth, boron, chromium, iron, magnesium, manganese, silicon, sodium, and tin) were at a level of less than 10 ppm each.

The effect of impurities on our measurements was modeled using tabulated values of the mass-attenuation coefficient [6]. A worst case scenario was modelled for the 99.99% pure samples, where the sample was assumed to contain an unusually large amount of high-Z impurities. The foils were assumed to be contaminated with 100 ppm lead and 50 ppm silver, representing a total contamination 50% higher than the maximum expected value. For 20 keV x rays this level of contamination produced an insignificant change in the mass-attenuation coefficient of 0.01%. The modelled effect of impurities was largest just below the edge where the mass-attenuation coefficient changed by up to 0.05%. The uncertainty contribution to the mass-attenuation coefficient due to impurities was included assuming the worst case scenario described above but was not significant at any energy.

B. Harmonics

A synchrotron beam contains a spectrum of energies. In most experiments the beam is passed through a monochromator in order to select the desired energy from the spectrum. However, the monochromation process is never perfect and the resultant beam may contain higher harmonic energies [32]. In this experiment, a monolithic silicon 111 double-crystal monochromator was used that allowed through odd multiples of the fundamental energy. In spite of detuning, we indeed detected the presence of two energies–the fundamental and third harmonic.

We determined the effective harmonic content at every measurement energy by measuring the attenuation of 15 aluminium foils with thicknesses ranging from 10 to 4000 μm that were mounted around the perimeter of the daisy wheels. The method of analysis used was similar to that of Ref. [32], where a detailed description can be found. Significant harmonic content was detected below 8 keV and is plotted in Fig. 8.

A correction was applied to the measured mass-attenuation coefficient based on the determined harmonic content in the beam. The magnitude of the correction was calculated using values of the aluminium mass-attenuation coefficient taken from the FFAST tabulation [7]. The correction was thickness dependent and was up to 0.4% for the thickest sample at 5 keV. The uncertainty contribution was calculated based on the uncertainty in the determined harmonic content and assuming an uncertainty of 5% in the FFAST tabulation. This uncertainty due to harmonics was only significant for the three lowest energies in the experiment where it contributed no more than 0.11%.

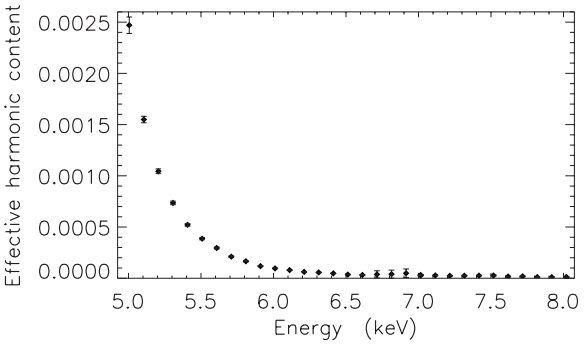

FIG. 8. The effective harmonic content was determined at every measurement energy and is plotted between 5 and 8 keV. Above 8 keV, the effective harmonic content did not differ significantly from zero.

The effective harmonic content can be converted to the more fundamental harmonic photon percentage. The harmonic photons percentage increased as the energy was decreased and was highest at 5 keV where $(0.103 \pm 0.004)\%$ of the x rays in the synchrotron beam were harmonic photons of energy 15 keV.

C. Saturation

Data collected at 11 and 12 keV were affected by "counter saturation" in the upstream ion chamber. Counter saturation occurs when the ion chamber amplification is too high and leads to the ion chamber signal becoming capped at a maximum value (in this case 10^6 counts pers) [9].

The upstream ion chamber signal varied quite smoothly against energy so that it was possible to recover the saturated ion chamber readings. The average value of the upstream ion chamber is plotted against energy between 13 and 16 keV in Fig. 9. The data point at 10 keV was included after correct-

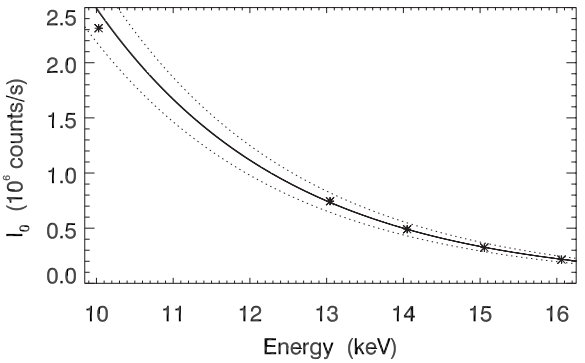

FIG. 9. The average value of the upstream ion chamber in units of millions of counts per second is plotted against energy. An exponential model was fitted to the data and is plotted as a solid line along with the uncertainty (dotted line).

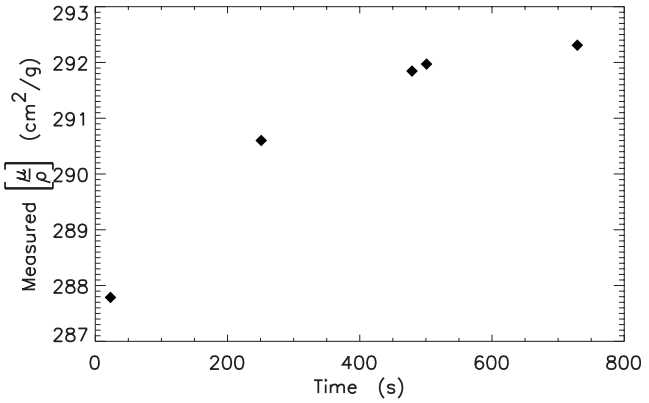

FIG. 10. The measured mass-attenuation coefficient is plotted against the time since the last monochromator change for a nominal energy of 9008 eV. The measured attenuation is increasing as the energy drifts downwards because the gradient of the mass-attenuation coefficient is negative in the region around 9008 eV.

ing for an amplifier gain change that reduced the count-rate by a factor of ten. An exponential model with two parameters was fitted to the data and the resultant line of best fit and uncertainties are plotted in Fig. 9. The count rates in the upstream ion chamber at 11 and 12 keV were determined using this model.

Measurements of the relative mass-attenuation coefficient were successfully recovered from the saturated data using the interpolated upstream ion chamber current. The saturation recovery process and the consequent loss of correlation between the two ion chambers lead naturally to relatively large uncertainties of the recovered relative mass-attenuation coefficient measurements. The recovered measurements were around 100 times less accurate than similar unsaturated measurements but remain valuable since no other measurements were available at these two energies.

D. Energy drift

There is a strong systematic effect in our data in the edge and XAFS regions that is caused by a consistent drift of the x-ray energy. Energy drift was seen whenever the monochromator angle was altered and had a time constant of several hundred seconds. This slow drift in the x-ray energy was not reflected in the nominal energy calculated from the monochromator angle encoder reading. The observed effect of energy drift had an exponential form as a function of the time after an energy change and is plotted in Fig. 10.

Energy drift can occur when there is a change in the heat load of a region of the monochromator [42]. Previous characterisation of energy drift induced by changes in the heat load show that it follows an exponential form with a time constant that can reach hours [43]. The energy drift could also have been caused by a weak physical link between the crystal and the motor that might cause overdamped mechanical drift of the monochromator angle.

The change in the measured mass-attenuation coefficient $\Delta_{[\frac{\mu}{\rho}]}$ due to energy drift can be described by the equation

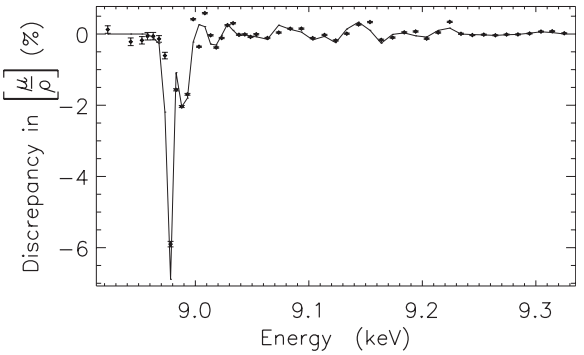

FIG. 11. The difference in mass-attenuation coefficient measured at two different times is plotted against energy for the 10 μm sample. The measurements were taken approximately 480 s apart at most energies. The modeled discrepancy due to energy drift is plotted as a solid line and fits the measured discrepancy well.

$$\Delta_{[\mu/\rho]} = \Delta_E \frac{\partial\left[\frac{\mu}{\rho}\right]}{\partial E}, \tag{4}$$

where Δ_E is the energy drift and $\frac{\partial[\frac{\mu}{\rho}]}{\partial E}$ is the gradient of the mass-attenuation coefficient with respect to energy.

In Fig. 10, the measured mass-attenuation coefficient is plotted against the time since the last monochromator change for a nominal energy of 9008 eV. The measured attenuation increased as the energy drifted lower. The time dependence indicates that the x-ray energy exponentially approached a stable value with a time constant of approximately 500 s.

An exponential model of the energy drift was developed with two parameters. One described the energy drift at $t=0$ and the other was a time constant. The initial energy drift was assumed to be linearly dependent on the magnitude of the last monochromator change.

This model was fitted to the data using a Levenberg-Marquardt nonlinear least-squares fitting routine yielding best-fit parameters and uncertainties. The time constant was found to be 470 ± 100 s while the magnitude of the energy drift was fitted to be 0.1176 ± 0.0098 of the previous monochromator change. The fitted model described the structure of the discrepancy well (see Fig. 11).

The best-fit model was used to correct for the effect of energy drift on the mass-attenuation coefficient measurements. This correction projected the measurements affected by energy drift onto the energy of the measurement made at the latest time. Hence we were able to assess the size of the effect and the robustness of the correction. The solid line in Fig. 11 was calculated using this correction and shows that the effect of energy drift was well accounted for. This correction was large (up to 16%) particularly for measurements made in the edge region taken shortly after a monochromator change. Outside the XAFS and edge regions the effect of energy drift was negligible due to the vanishing gradient.

The uncertainty in the mass-attenuation coefficient due to energy drift was calculated from the fitted parameter uncertainties. The uncertainty in the mass-attenuation coefficient due to energy drift was between 0.1 and 0.5 % in the XAFS

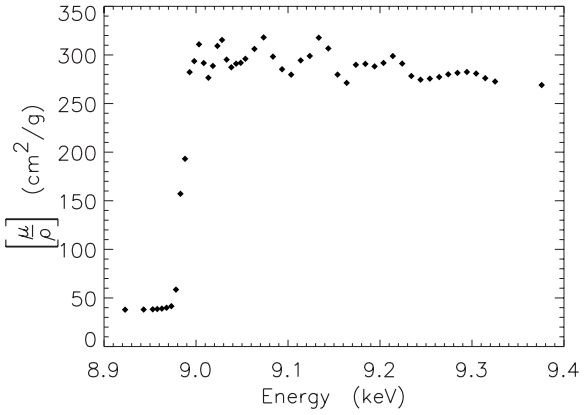

FIG. 12. The absorption edge and fine structure (XAFS) can be seen in the mass-attenuation coefficient between 8.9 and 9.4 keV. The uncertainties in these measurements are too small to be plotted as error bars on the scale of this graph.

region and between 0.5 and 1.3 % in the edge region and is the limiting error for most measurements in these two regions.

E. Other systematics

The XERT has previously been used to determine the bandwidth of a synchrotron beam by measuring the thickness dependence of the attenuation of samples at the absorption edge [31]. We employed the same technique and produced a null result for bandwidth. This implies that—in this experiment—the effect of bandwidth was much less significant than that of energy drift. Bandwidth has its greatest effect on attenuation measurements in the XAFS and edge regions where there is a large uncertainty caused by energy drift in our data. Relative to the size of the energy-drift uncertainty, the effect of bandwidth was insignificant.

Some previous XERT experiments have observed a systematic error due to fluorescence radiation and scattering [30] (other XERT experiments did not [9,11]). These effects were modeled but did not improve the self consistency of our data. The effect of fluorescence radiation and scattering was therefore negligible in this experiment.

VI. TABULATION OF RESULTS

Table III presents measurements of the mass-attenuation coefficient as well as the imaginary component of the form factor f'' at 108 energies between 5 and 20 keV. At each energy the mass-attenuation coefficient was determined by a weighted mean of the measurements taken on all samples and apertures. Figure 12 plots the mass-attenuation coefficient in the region of the absorption edge and XAFS between 8.9 and 9.4 keV.

The imaginary component of the form factor quantifies the photoelectric absorption of a material. Photoelectric absorption is the dominant contributor to the x-ray mass-attenuation coefficient for copper for the energies in Table III, with scattering contributing less than 5%. The photoelectric mass-absorption was calculated from the measured total mass-attenuation coefficient by subtracting the contribution to the attenuation due to Rayleigh and Compton scattering.

The scattering contribution was calculated by taking the average of the FFAST [6] and XCOM [8] tabulations of the Rayleigh plus Compton attenuation coefficient with the resultant uncertainty assumed to be the difference between the two tabulations divided by $\sqrt{2}$. The scattering uncertainty contributed between 0.05 and 0.13 % to the photoelectric absorption and is only significant in the region just below the edge.

The imaginary component of the atomic form factor f'' was calculated using

$$f'' = \frac{m_a}{2hcr_e}\left[\frac{\mu}{\rho}\right]_{PE}, \tag{5}$$

where $\left[\frac{\mu}{\rho}\right]_{PE}$ is the photoelectric attenuation coefficient, m_a is the atomic mass, r_e is the classical electron radius, h is Planck's constant, and c is the speed of light [44].

This paper used samples of metallic (solid-state) copper, but are an excellent approximation to the atomic result outside the edge regions. The equivalence of solid-state and atomic mass-attenuation coefficient outside the edge and XAFS regions has been suggested and illustrated for cadmium [12]. Therefore, our measurement of the form factor can be viewed as approximating the atomic form factor of copper, except at the edge and in the XAFS region between 8.9 and 9.5 keV where solid-state effects are dominant.

Measurements of the mass-attenuation coefficient prove useful for XAFS and as a standard XAFS spectrum. XAFS analysis does not require absolute measurements of the mass-attenuation coefficient; for current modeling it conventionally requires high-accuracy relative measurements. Therefore the uncertainty due to the absolute thickness determination (0.092%) can be subtracted from the total uncertainty when the data from Table III is used in XAFS analyses. The uncertainty in the mass-attenuation coefficient was dominated by the contribution due to the absolute calibration, so subtracting this reduces the uncertainty greatly.

The first column of Table III gives the calibrated x-ray energy in keV and the uncertainty in the last significant digit(s) is given in brackets. Column two tabulates the value of the mass-attenuation coefficient in cm^2/g with the uncertainty in brackets. Column three gives the uncertainty in the mass-attenuation coefficient as a percentage of its value. The fourth column lists the imaginary component of the form factor along with its uncertainty in brackets. A breakdown of the contributions to the uncertainty of the energy, mass-attenuation coefficient and imaginary component of the form factor is given in Table IV.

VII. COMPARISON WITH OTHER MEASUREMENTS AND THEORY

It is instructive to compare the new results of this paper with previous measurements. Our results show excellent agreement with those of Chantler *et al.* [13] across the entire common energy range (Fig. 13). Despite the small uncertainties of both datasets (0.33% median uncertainty for Chantler

TABLE IV. A breakdown of the uncertainty contributions to the mass-attenuation coefficient, imaginary component of the form factor, and the energy.

Quantity	Uncertainty	Comment
$[\frac{\mu}{\rho}]$	0.092%	Accuracy of the full-foil mapping
	<0.11%	5.0–5.3 keV due to harmonics
	<1.4%	Uncertainty due to energy drift in the edge and XAFS region
	4%	at 11 and 12 keV due to saturation
f''	0.09–4.5%	Contribution from $[\frac{\mu}{\rho}]$
	<0.15%	Scattering contribution uncertainty, largest just below edge
Energy	0.3–0.6 eV	Accuracy limited by powder diffraction results
	<0.15 eV	Energy drift uncertainty between 8 and 10 keV

et al. [13]), the χ_r^2 between them is 0.62. The two experiments were performed at the same beam line, but with different beam optics. It is notable that these two experiments used a different method for the absolute calibration of the mass-attenuation coefficient (full foil vs partial foil). Also, a number of the copper foil samples used in this experiment were not used in the earlier experiment, including one of the foils used for the absolute calibration. The excellent agreement of these two datasets suggests that with good experimental technique, careful consideration of systematic errors and proper treatment of uncertainties, one can produce high-accuracy measurements of the mass-attenuation coefficient with realistic uncertainty estimates.

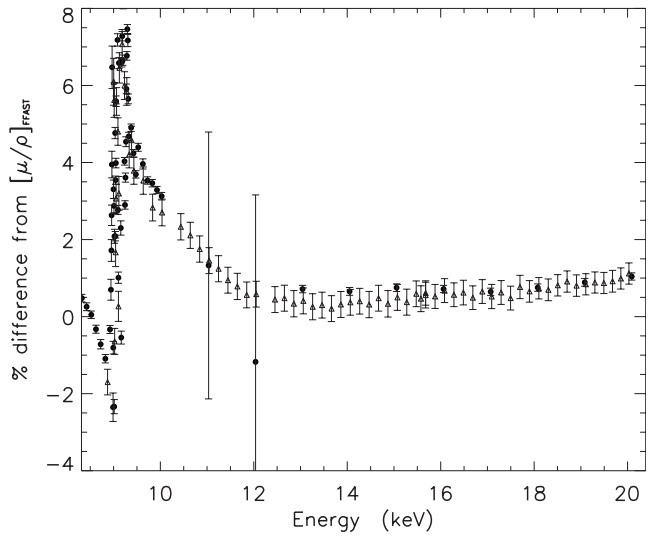

FIG. 13. A comparison of the results of the present work (plotted as filled circles) with those of Chantler *et al.* [13] (plotted as open triangles). The plot shows the percentage difference between the measured mass-attenuation coefficient and the FFAST tabulation. The scatter of the data points between 9 and 10 keV is mainly caused by the fine structure in the attenuation coefficient (i.e., XAFS). The results of the two experiments are in excellent agreement with one another.

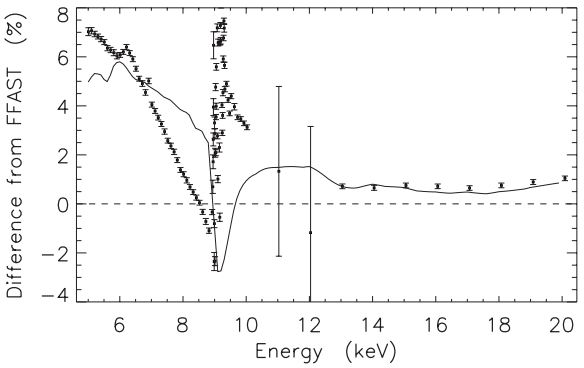

FIG. 14. Percentage discrepancy between the results presented in this work and the major theoretical tabulations of the mass-attenuation coefficient. The data is presented as the percentage difference from the FFAST tabulation. The results of this work are plotted with error bars, the XCOM tabulation is plotted as a solid line and the FFAST tabulation is the dashed line. The scatter of the data points between 9 keV and 10 keV is the result of comparing an atomic calculation with a solid-state measurement (i.e., XAFS).

We also compared our results to all the measurements presented in Fig. 1. Most of these previous measurements did not have an equivalent measurement in this work, so each point was interpolated to the nearest energy in our dataset. Of the twelve datasets with more than two measurements in the energy range 5 and 20 keV, only four are in reasonable agreement with the present work: Parthasaradhi, $\chi_r^2=1.8$ (four energies); Murty *et al.*, $\chi_r^2=1.0$ (five energies); Sandiago *et al.*, $\chi_r^2=0.3$ (five energies); and Chantler *et al.*, $\chi_r^2=0.6$ (58 energies). It should be noted that the median uncertainties of the four datasets are 2.0, 1.0, 3.0, and 0.33 %, respectively. Only Murty *et al.* and Chantler *et al.* agree with the present work and have uncertainties at or below 1%.

Below the *K* edge there have been no experiments of similar accuracy to the present work. Of the seven datasets with more than two points in the energy range 5 to 8.9 keV, only Hopkins *et al.* [15] and Sandiago *et al.* [26] are in any agreement with the present work (a χ_r^2 of less than 5 within that energy range).

It is interesting to compare our measurements of the mass-attenuation coefficient of copper with earlier theoretical tabulations. A comparison with the two theoretical tabulations recommended by NIST is given in Fig. 14. Far above the absorption edge both the FFAST and XCOM tabulations agree with the experimental data to within 1%, corresponding to their estimated uncertainty. In fact XCOM agrees to within two times the experimental uncertainty (or about 0.3%) in this region. The current data also agrees with the FFAST tabulation to within its own uncertainty estimates of 10% just above the *K* edge and 1% far from the *K* edge [6,7].

A large and systematic difference of up to 8% (FFAST) and 10% (XCOM) exists between our measurements and the theoretical tabulations in a region that extends several keV above the copper *K* edge. The theoretical value is much lower than the experimental value, with the discrepancy increasing as the *K* edge is approached. Similar discrepancies

have been observed above the *K* edges of silver [10], molybdenum [9], and tin [11]. Of particular interest is the fact that Kodre *et al.* [12] observed a similar discrepancy in both solid and vapourous cadmium, suggesting that solid-state effects are not the cause of this discrepancy. The disagreement between the two theoretical results also points to a theoretical origin for this systematic difference with experiment.

Between the edge and 7.5 keV, FFAST appears more accurate with a discrepancy of about 1% corresponding to the claimed theoretical uncertainty. However, the trend for both tabulations in this region is not consistent and suggests that greater theoretical investigation of this system is required.

Below 7.5 keV, the FFAST tabulation appears to have a smooth but slowly increasing discrepancy towards softer energies. The XCOM tabulation is consistently 1–3 % different from experiment and agrees better in this region.

The availability of high accuracy measurements of the mass-attenuation coefficient, such as those presented in this work are challenging the predictive power of the current theoretical tabulations. The current theoretical tabulations of attenuation coefficients and form factors have been shown to need further investigation, particularly near absorption edges. In the time since these tabulations were published, computing power has increased by an order of magnitude. An opportunity exists to make use of this computer power to produce new tabulations that challenge the accuracy achievable using current experimental techniques.

VIII. CONCLUSION

The x-ray mass-attenuation coefficient and imaginary component of the form factor of copper was measured at 108 energies between 5 and 20 keV. The accuracy of the measurements ranged between 0.09 and 4.5 % with most points being accurate to between 0.09 and 0.12 %.

There were a number of systematic errors present in the data that were observed and—where possible—corrected for. Subsets of the experimental data were effected by harmonics, ion chamber saturation, energy drift, and impurities in the sample.

Comparison of our results with previous measurements revealed deficiencies in previously published experimental results. In particular, a poor or nonexistant consideration of systematic errors as well as the underestimation of experimental uncertainties are common failings of past datasets. The results of this paper were also compared with theory, exposing some inadequacies in current tabulations.

ACKNOWLEDGMENTS

We wish to acknowledge developmental work of Martin D. de Jonge on XERT analysis techniques including the full-foil mapping technique. We also wish to acknowledge the assistance of the beamline staff, Garry Foran and David Cookson, during the experiment at the Photon Factory (ANBF). This work was supported by the Australian Synchrotron Research Program, which is funded by the Commonwealth of Australia under the Major National Research Facilities Program, and by grants of the Australian Research Council.

[1] W. C. Röntgen, Sitzungsber. Physmed. Ges. Würzburg **137**, 132 (1895).
[2] I. Coulthard and T. K. Sham, Phys. Rev. Lett. **77**, 4824 (1996).
[3] S. S. Hasnain, J. R. Helliwell, and H. Kamitsubo, J. Synchrotron Radiat. **6**, 121 (1999).
[4] P. Palmberg and T. Rhodin, J. Appl. Phys. **39**, 2425 (1968).
[5] S. Bohic, A. Simionovici, A. Snigirev, R. Ortega, G. Devès, D. Heymann, and C. Schroer, Appl. Phys. Lett. **78**, 3544 (2001).
[6] C. T. Chantler, J. Phys. Chem. Ref. Data **29**, 597 (2000).
[7] C. T. Chantler, K. Olsen, R. A. Dragoset, J. Chang, A. R. Kishore, S. A. Kotochigova, and D. S. Zucker, http://physics.nist.gov/ffast
[8] M. Berger, J. Hubbell, S. Seltzer, J. Coursey, and D. Zucker (unpublished).
[9] M. D. de Jonge, C. Q. Tran, C. T. Chantler, Z. Barnea, B. B. Dhal, D. J. Cookson, W.-K. Lee, and A. Mashayekhi, Phys. Rev. A **71**, 032702 (2005).
[10] C. Q. Tran, C. T. Chantler, Z. Barnea, M. D. de Jonge, B. B. Dhal, C. T. Y. Chung, D. Paterson, and J. Wang, J. Phys. B **38**, 89 (2005).
[11] M. de Jonge *et al.*, Phys. Rev. A **75**, 032702 (2007).
[12] A. Kodre, J. Padežnik Gomilšek, A. Mihelič, and I. Arčon, Radiat. Phys. Chem. **75**, 188 (2006).
[13] C. T. Chantler, C. Q. Tran, Z. Barnea, D. Paterson, D. J. Cookson, and D. X. Balaic, Phys. Rev. A **64**, 062506 (2001).
[14] V. R. K. Murty, K. S. Rao, G. Arunaprasad, K. Parthasaradhi, J. R. Rao, and V. Lakshminarayana, Lett. Nuovo Cimento Soc. Ital. Fis. **39**, 125 (1977).
[15] J. I. Hopkins, J. Appl. Phys. **30**, 185 (1959).
[16] M. J. Cooper, Acta Crystallogr. **18**, 813 (1965).
[17] A. J. Bearden, J. Appl. Phys. **37**, 1681 (1966).
[18] G. D. Hughes, J. B. Woodhouse, and I. A. Bucklow, Br. J. Appl. Phys. **1**, 695 (1968).
[19] K. Parthasaradhi and H. H. Hansen, Phys. Rev. A **10**, 563 (1974).
[20] V. V. Rao and Shahnawaz, Lett. Nuovo Cimento Soc. Ital. Fis. **44**, 181 (1978).
[21] K. S. Puttaswamy, R. Gowda, and B. Sanjeevaiah, Can. J. Phys. **57**, 92 (1979).
[22] R. Nathuram, I. S. Sundara Rao, and M. K. Mehta, Phys. Rev. A **37**, 4978 (1988).
[23] L. Unonius and P. Suortti, Can. J. Phys. **22**, 46 (1989).
[24] W. Dachun, D. Xunliang, W. Xinfu, Y. Hua, Z. Hongyu, S. Xinyin, and Z. Guanghua, Nucl. Instrum. Methods Phys. Res. B **71**, 241 (1992).
[25] A. A. Tajuddin, C. S. Chong, A. Shukri, T. Bandyopadhyay, and D. A. Bradley, Appl. Radiat. Isot. **46**, 113 (1995).
[26] Sandiago, T. K. Umesh, and R. Gowda, Pramana **48**, 1077

(1997).
[27] D. C. Creagh and J. H. Hubbell, Acta Crystallogr., Sect. A: Found. Crystallogr. **43**, 102 (1987).
[28] D. Creagh and J. Hubbell, Acta Crystallogr., Sect. A: Found. Crystallogr. **108**, 7673 (1999).
[29] C. Q. Tran, C. T. Chantler, and Z. Barnea, Phys. Rev. Lett. **90**, 257401 (2003).
[30] C. Q. Tran, M. D. de Jonge, Z. Barnea, and C. T. Chantler, J. Phys. B **37**, 3163 (2004).
[31] M. D. de Jonge, Z. Barnea, C. Q. Tran, and C. T. Chantler, Phys. Rev. A **69**, 022717 (2004).
[32] C. Q. Tran, Z. Barnea, M. D. de Jonge, B. B. Dhal, D. Paterson, D. J. Cookson, and C. T. Chantler, X-Ray Spectrom. **32**, 69 (2003).
[33] Z. Barnea, D. C. Creagh, T. J. Davis, R. F. Garrett, S. Janky, A. W. Stevenson, and S. W. Wilkins, Rev. Sci. Instrum. **63**, 1069 (1992).
[34] A. J. C. Wilson and E. Prince, *International Tables for Crystallography* (Kluwer, London, 1999), Vol. C.
[35] S. Rasberry, C. Hubbard, Y. Zhang, and R. McKenzie, *Standard Reference Material Certificates, Standard Reference Material 660, NIST* (NIST, Gaithersburg, MD, 1989).
[36] C. Chantler, C. Tran, D. Paterson, Z. Barnea, and D. Cookson, X-Ray Spectrom. **29**, 449 (2000).
[37] C. Chantler, C. Tran, D. Paterson, D. Cookson, and Z. Barnea, X-Ray Spectrom. **29**, 459 (2000).
[38] B. Nordfors, Ark. Fys. **18**, 37 (1960).
[39] N. A. Rae, C. T. Chantler, C. Q. Tran, and Z. Barnea, Radiat. Phys. Chem. **75**, 2063 (2006).
[40] M. D. de Jonge, Z. Barnea, C. Q. Tran, and C. T. Chantler, Meas. Sci. Technol. **15**, 1811 (2004).
[41] C. Q. Tran, C. T. Chantler, Z. Barnea, and M. D. de Jonge, Rev. Sci. Instrum. **75**, 2943 (2004).
[42] G. Evans and R. Pettifer, Rev. Sci. Instrum. **67**, 3428 (1996).
[43] M. Watanabe, A. Toyoshima, J. Adachi, and A. Yagishita, Nucl. Instrum. Methods Phys. Res. A **467–468**, 512 (2001).
[44] P. Mohr and B. Taylor, Rev. Mod. Phys. **72**, 351 (2000).